nature climate change

SUPPLEMENTARY INFORMATION

DOI: 10.1038/NCLIMATE3056

Human-induced greening of the northern extratropical land surface

Jiafu Mao[1†], Aurélien Ribes[2], Binyan Yan[3], Xiaoying Shi[1], Peter E. Thornton[1], Roland Séférian[2], Philippe Ciais[4], Ranga B. Myneni[5], Hervé Douville[2], Shilong Piao[6,7,8], Zaichun Zhu[6], Robert E. Dickinson[3], Yongjiu Dai[9], Daniel M. Ricciuto[1], Mingzhou Jin[10], Forrest M. Hoffman[11], Bin Wang[12,13], Mengtian Huang[6], and Xu Lian[6]

[1] Environmental Sciences Division and Climate Change Science Institute, Oak Ridge National Laboratory, Oak Ridge, TN, USA
[2] Centre National de Recherches Météorologiques, Météo-France/CNRS, 42 Avenue Gaspard Coriolis, 31057 Toulouse, France
[3] Jackson School of Geosciences, the University of Texas, Austin, TX, USA
[4] Laboratoire des Sciences du Climat et de l'Environnement, LSCE, 91191 Gif sur Yvette, France
[5] Department of Earth and Environment, Boston University, Boston, MA 02215, USA
[6] Sino-French Institute for Earth System Science, College of Urban and Environmental Sciences, Peking University, Beijing 100871, China
[7] Key Laboratory of Alpine Ecology and Biodiversity, Institute of Tibetan Plateau Research, Chinese Academy of Sciences, Beijing 100085, China.
[8] CAS Center for Excellence in Tibetan Plateau Earth Science, Beijing 100085, China
[9] College of Global Change and Earth System Science, Beijing Normal University, Beijing, China
[10] Department of Industrial and Systems Engineering, University of Tennessee, Knoxville, TN, USA
[11] Computer Science and Mathematics Division and Climate Change Science Institute, Oak Ridge National Laboratory, Oak Ridge, TN 37831, USA
[12] State Key Laboratory of Numerical Modeling for Atmospheric Sciences and Geophysical Fluid Dynamics, Institute of Atmospheric Physics, Beijing 100029, China
[13] Center for Earth System Science, Tsinghua University, Beijing 100084, China

Supporting Online Material

Datasets and Method

(1) GIMMS LAI3g and GEOLAND2 LAI data

The Global Inventory Modeling and Mapping Studies (GIMMS) LAI3g[1] dataset, spanning from July 1981 to December 2011 at the temporal resolution of 15 days and covering the globe at 1/12 degree spatial resolution, has been recently published. This product was generated using a neural network trained by GIMMS NDVI3g and filtered MODIS Leaf Area Index (LAI) products during the overlapping years. The GEOLAND2 project (http://www.copernicus.eu/projects/geoland2) developed a 30-year LAI product (1982 to present) with 10-day temporal resolution and 1/122° (about 1 km at the equator) spatial resolution[2]. Based on the neural network approach, this product was obtained from a combination of two sensors, NOAA-AVHRR (1982~1999) and SPOT-VGT (1999~present). The first component of the product was obtained from NOAA-AVHRR. The second component of the product, GEOLAND2/BioPar GEOV1 LAI, was developed from the SPOT/VGT sensor; it is distributed at http://land.copernicus.eu/global/. Both the LAI3g and GEOLAND2 LAI have been extensively evaluated with field measurements and other remote-sensing-based products, in terms of the mean states, multiyear variations, and responses to climate change. For model evaluations, environmental monitoring and assessment, and vegetation dynamics studies, the suitability of each has also been well documented and assessed[1-7].

To more easily compare satellite LAI time series with earth system model (ESM) simulations, which have no gaps, and to consistently apply the growing season definition for observed and modeled LAI, we filled the gaps of the two LAI products. Gaps in both remote-sensing LAI time series resulting from the cloud coverage, algorithm failure, or low quality of source reflectance were filled following common practice published in previous work[8,9]. Generally, the short gaps (shorter than one year) were first filled using a cubic curve fitting according to the following criteria: (1) at least 35.0% of the data for the year are not missing, and (2) the gap is not located at the beginning or ending of the year. A 12-month window starting at any day of a year, instead of January 1 to December 31, was moved around the gap to be filled to obtain a “best” location for curve fitting. The “best” here refers to the condition that satisfies the above criteria and that contains the highest percentage of non-missing values. Long gaps were then filled using the climatological mean. Resultant data were then remapped to a coarser spatial resolution (2°×2°) for detection and attribution. The decrease of pixel size toward the poles due to the curvature of the earth was considered in the spatial resampling process. Similar to that documented in ref. 10, the annual growing season LAIs were derived by averaging the LAIs of growing-season months, which are defined as April–October, May–October, or May–September within a given year.

(2) Prognostic LAI of CMIP5 models

We used monthly mean LAI results from 19 fully-coupled ESMs participating in the CMIP5 project[11] (Table S1). They comprise a set of simulations: ALL, with historical anthropogenic and natural forcings (solar variability and volcanic aerosols as well as well-mixed greenhouse gases plus other anthropogenic factors such as aerosols, land use/land cover change (LULCC) and/or ozone), GHG, with greenhouse gases forcing only (anthropogenic well-mixed greenhouse gases), NAT, with natural forcings only (solar variability and volcanic aerosols), and unforced preindustrial control simulations (CTL, internal variability only).

Since not all models provide historical simulations extending to year 2011, the Representative Concentration Pathway (RCP) 4.5 simulations were used to extend the ALL simulations over the years 2006 to 2011. To discuss the possible impacts of CO_2 fertilization and greenhouse gas radiative effects on the LAI dynamics, we also analyzed the esmFixClim2 (radiation code sees constant CO_2 concentration of year 1850, but carbon cycle sees historical followed by RCP4.5 rise in CO_2) and esmFdbk2 (carbon cycle sees constant CO_2 concentration of year 1850, but radiation sees historical followed by RCP4.5 rise in CO_2) experiments. Results were shown from 18 models and 43 runs for ALL, 6 models and 17 runs for NAT, 5 models and 15 runs for GHG, 6 models and 6 runs for esmFixClim2, and 4 models and 4 runs for esmFdbk2.

The multi-realization mean of each model/forcing was used for analysis. The simulations were resampled to a 2°×2° spatial resolution. The regional mean growing-season LAIs were calculated for each model/forcing group according to the growing season definition using the same approach as the satellite observations for all historical simulations. Based on the annual time series of the regionally averaged growing-season LAIs, 3-year averaged LAIs were calculated, resulting in 10 time steps for the 1982–2011 period. The CTL simulations contain LAI time series with different lengths up to 1000 years, corresponding to multiple 30-year segments.

(3) Comparison of observed and simulated LAI trends

The statistical tests used to compare observed and simulated trends (the fourth paragraph of the main text) are chi-square tests constructed as follows. We assume *n* simulations (either unforced 30-year segments or individual historical simulations) $x_1,..., x_n$ are available, independent, and identically distributed, following a Gaussian distribution. We wonder whether the observed value *y* is consistent with the distribution of the x_i. The statistical test we used is derived from

$$(y-\bar{x}) \backsim N(0,(1+1/n)\sigma^2)$$

where $\overline{x}$ is the sample mean of the (x_i). This test is based on the statistic

$$s=\frac{n}{n+1}\frac{(y-\bar{x})^2}{\hat{\sigma}^2} \sim F(1,n-1)$$

Confidence intervals on model-simulated trends are computed with the same approach, at the 90% level.

(4) Robustness of detection to inflated IV assumptions

The rejection of the residual consistency test (RCT), which was found in most cases, might be related to an underestimation of IV by current ESMs. In order to address this possible weakness of our analysis, we investigated the robustness of our results to using inflated estimates of IV. In that investigation, the covariance structure is still estimated from climate model CTL simulations, but its magnitude is revised and inflated.

This test is done in a simplified statistical framework where the response pattern is assumed to be known and linear in time (i.e., the response pattern simulated by climate models is not used). In this way, we study the significance of the linear trend. The multi-model mean response shown in Fig. 2 is very close to being linear over the 30-year period. The statistical regression model is then fitted using an ordinary least square (OLS) algorithm[12,13] where the expected response X* is considered as being known, related to the following two reasons. First, one approach used here (case Lin_Σobs) is to estimate the magnitude of the variance in $\sum$ directly from the observed data. This cannot be done under total least square (TLS), as TLS requires the ratio of variances in $\sum$ and $\sum_X$ to be known[14]. Second, the use of the TLS approach is not required if a fixed response pattern is assumed, as is done here with a time-linear response. Such a parametric assumption is, at worst, suboptimal, and may reduce the chance to successfully detect a change.

The results obtained with this sensitivity analysis are shown in Fig. S5 for the April to October mean LAI (consistent with the main text and Fig. 4), and in Fig. S6 for alternative seasons. In terms of attributable trend, the results obtained using this simpler method, and an estimate of IV derived from model simulations (Lin_Σmod in Fig. S5), are very close to those found with the Multi1 ALL response (Fig. 4). When the magnitude of IV is estimated from observations instead of from climate models (Lin_Σobs, Fig. S5), the estimated variance is about 2.5 times larger, and the confidence intervals on the scaling factors are widened. However, the detection of the response to external forcings (i.e., $\beta \neq 0$) remains very clear. The most important difference caused by the inflated IV comes from the RCT, which is then well passed. This enhances confidence in our result, as detection is shown to be robust if a higher, observationally based estimate of IV is considered. To further our investigation, we apply the same method using a simulated variance inflated by a factor of 8 (Lin_8×Σmod, Fig. S5). With such a large inflation of IV, the (2-sided) RCT is rejected again, but this time because the regression residuals are found to be significantly smaller than expected when such a large IV is assumed. In this way, we are dealing with an upper bound of internal variability. Detection is still found to be significant, although barely. This again strengthens confidence in the detection of recent LAI changes.

References

1. Zhu, Z. *et al.* Global data sets of vegetation leaf area index (LAI) 3g and fraction of photosynthetically active radiation (FPAR) 3g derived from global inventory modeling and mapping studies (GIMMS) normalized difference vegetation index (NDVI3g) for the period 1981 to 2011. *Rem. Sens.* **5,** 927–948 (2013).
2. Baret, F. *et al.* GEOV1: LAI and FAPAR essential climate variables and FCOVER global time series capitalizing over existing products. part1: Principles of development and production. *Rem. Sens. Environ.* **137,** 299–309 (2013).
3. Camacho, F. *et al.* GEOV1: LAI, FAPAR essential climate variables and FCOVER global time series capitalizing over existing products. Part 2: Validation and intercomparison with reference products. *Rem. Sens. Environ.* **137,** 310–329 (2013).
4. Murray-Tortarolo, G. *et al.* Evaluation of land surface models in reproducing satellite-derived LAI over the high-latitude Northern Hemisphere. Part I: Uncoupled DGVMs, *Rem. Sens.* **5,** 4819–4838 (2013).
5. Anav, A. *et al*. Evaluation of land surface models in reproducing satellite derived leaf area index over the high-latitude northern hemisphere. part II: earth system models. *Rem. Sens.* **5,** 3637–3661 (2013).
6. Mahowald, N. *et al*. Projections of leaf area index in earth system models. *Earth Syst. Dynam.* **7,** 211–229, doi:10.5194/esd-7-211-2016 (2016).
7. Mao, J. *et al.* Global latitudinal-asymmetric vegetation growth trends and their driving mechanisms: 1982–2009. *Rem. Sens.* **5,** 1484–1497 (2013).
8. Verger A. *et al.* The CACAO method for smoothing, gap filling, and characterizing seasonal anomalies in satellite time series. *IEEE Trans. Geosci. Remote Sens.* **51,** 1963–1972 (2013).

9. Weiss, D. J. *et al.* An effective approach for gap-filling continental scale remotely sensed time-series. *Isprs Journal of Photogrammetry and Remote Sensing* **98,** 106–118 (2014).
10. Piao, S. *et al*. Evidence for a weakening relationship between interannual temperature variability and northern vegetation activity. *Nature Commun.* **5,** 5018 (2014).
11. Taylor,K. E., Stouffer, R. J. and Meehl, G. A. An overview of CMIP5 and the experiment design. *Bull. Amer. Meteor. Soc.* **93,** 485–498 (2012).
12. Allen, M. and Stott, P. Estimating signal amplitudes in optimal fingerprinting, part I: theory. *Clim. Dynam.* **21,** 477–491 (2003).
13. Ribes, A. Planton, S. and Terray, L. Application of regularised optimal fingerprinting to attribution. part I: method, properties and idealised analysis. *Clim. Dynam.* **41,** 2817–2836 (2013).
14. Wald, A. The fitting of straight lines if both variables are subject to error. *Ann. Math. Stat.* **11,** 284–300 (1940).

Table S1. The coupled model name, modeling center information, name of the land surface model in the coupled model, horizontal resolution (latitude/longitude) of the land surface model, nitrogen dynamics information of the land surface model, prognostic vegetation coverage information of the land surface model, length (years) of the preindustrial unforced control (CTL) simulations, the availability of CMIP5 simulations (historical) with anthropogenic and natural forcings (ALL), the availability of CMIP5 simulations (historicalNat) with natural forcings alone (NAT), the availability of CMIP5 simulations (historicalGHG) simulations with greenhouse gases forcings (GHG), the availability of CMIP5 simulations (esmFixClim2) with radiation code seeing constant CO_2 concentration of year 1850, but carbon cycle seeing historical followed by RCP4.5 rise in CO_2, the availability of CMIP5 simulations (esmFdbk2) carbon cycle seeing constant CO_2 concentration of year 1850, but radiation seeing historical followed by RCP4.5 rise in CO_2, and the availability of CMIP5 simulations (historicalMisc) with Land Use/Land Cover Change (LULCC) for 1982-2011.

Model	Modeling Group	Land Component	Land Resolution	N-cycle	Dynamic vegetation	piControl Length	historical (43)	historical Nat (17)	historical GHG (15)	esmFixClim2 (6)	esmFdbk2 (4)	historical Misc (5)
bcc-csm1-1	Beijing Climate Center, China Meteorological Administration, CHINA	BCC_AVIM1.0	2.875° × 2.875°	N	N	500	3	1	1	1	1	
bcc-csm1-1-m	Beijing Climate Center, China Meteorological Administration, CHINA	BCC_AVIM1.0	2.875° × 2.875°	N	N	400	3					
CanESM2	Canadian Center for Climate Modelling and Analysis, CANADA	CLASS2.7&CTEM1	2.81° × 2.81°	N	N	996	5	5	5	1	1	5
CCSM4	National Center for Atmospheric Research (NCAR), USA	CLM4	0.9° ×1.25°	Y	N	1051	6					
CESM1-BGC	Community Earth System Model Contributors, NSF-DOE-NCAR, USA	CLM4	0.9° ×1.25°	Y	N		1					
CESM1-CAM5	Community Earth System Model Contributors, NSF-DOE-NCAR, USA	CLM4	0.9° ×1.25°	Y	N	319	3					
CESM1-WACCM	Community Earth System Model Contributors, NSF-DOE-NCAR, USA	CLM4	0.9° ×1.25°	Y	N	200	3					
GFDL-ESM2M	NOAA Geophysical Fluid Dynamics Laboratory, USA	LM3	2.5° ×2.5°	N	Y	500				1		
HadGEM2-CC	Met Office Hadley Centre, UNITED KINDOM	JULES	1.25° ×1.875°	N	Y	240	1					
HadGEM2-ES	Met Office Hadley Centre, UNITED KINDOM	JULES	1.25° ×1.875°	N	Y	576	4	4	4	1	1	
IPSL-CM5A-LR	Institut Pierre-Simon Laplace, FRANCE	ORCHIDEE	3.75° ×1.9°	N	N	1000	4	3	4	1	1	
IPSL-CM5A-MR	Institut Pierre-Simon Laplace, FRANCE	ORCHIDEE	2.5° ×1.25°	N	N	300	1	3				
IPSL-CM5B-LR	Institut Pierre-Simon Laplace, FRANCE	ORCHIDEE	3.75° ×1.9°	N	N	300	1					
MIROC-ESM-CHEM	JAMSTEC, University of Tokyo, and NIES, JAPAN	MATSIRO & SEIB-DGVM	2.875° ×2.875°	N	Y	255	1					
MIROC-ESM	JAMSTEC, University of Tokyo, and NIES, JAPAN	MATSIRO & SEIB-DGVM	2.875° ×2.875°	N	Y	630	1			1		
MPI-ESM-LR	Max Planck Institute for Meteorology, GERMANY	JSBACH	1.9° ×1.9°	N	Y	1000	3					
MPI-ESM-MR	Max Planck Institute for Meteorology, GERMANY	JSBACH	1.9° ×1.9°	N	Y	1000	1					
NorESM1-ME	Norwegian Climate Centre, NORWAY	CLM4	1.9° ×2.5°	Y	N	252	1					
NorESM1-M	Norwegian Climate Centre, NORWAY	CLM4	1.9° ×2.5°	Y	N	501	1	1	1			

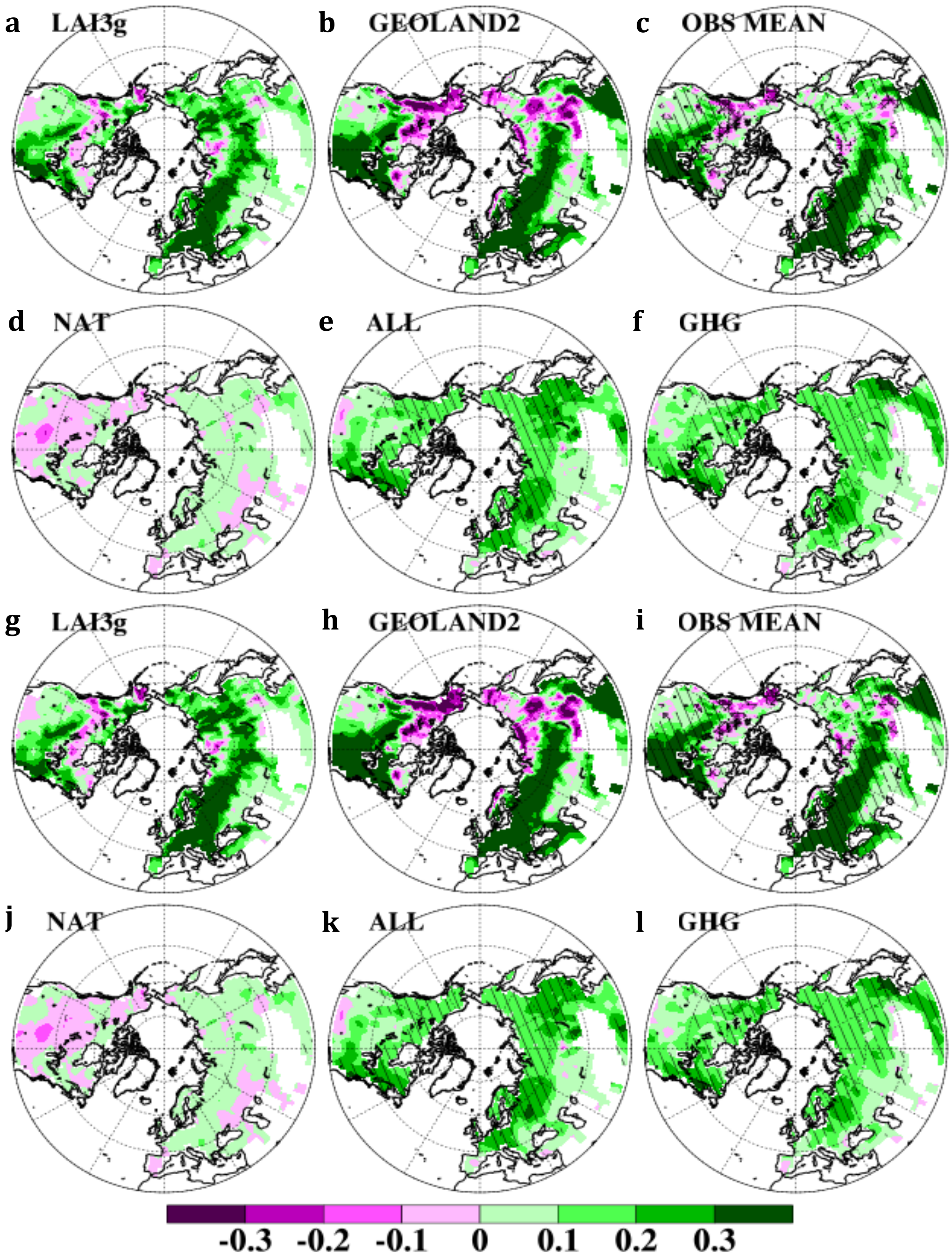

Figure S1. This figure is similar to Fig. 1, but it considers different definitions of the growing season LAI (a–f for May–October [M2O], g–l for May–September [M2S]).

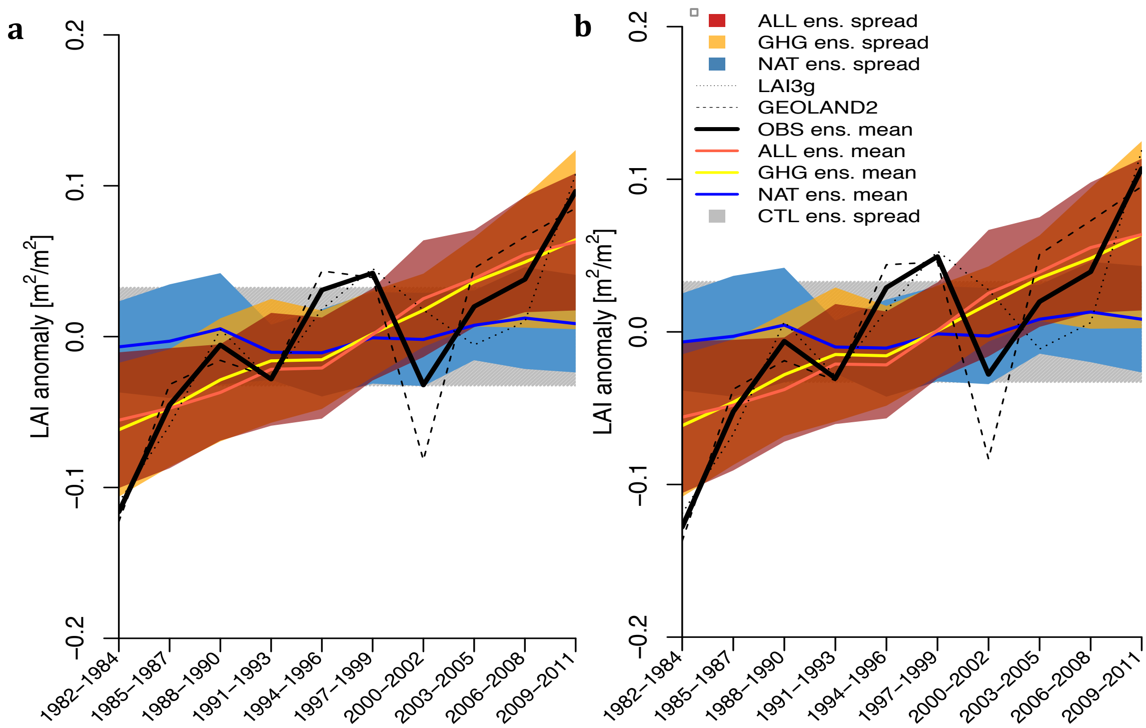

Figure S2. This is similar to Fig. 2, but it considers different definitions of the growing season LAI (a, for May–October [M2O], b for May–September [M2S]).

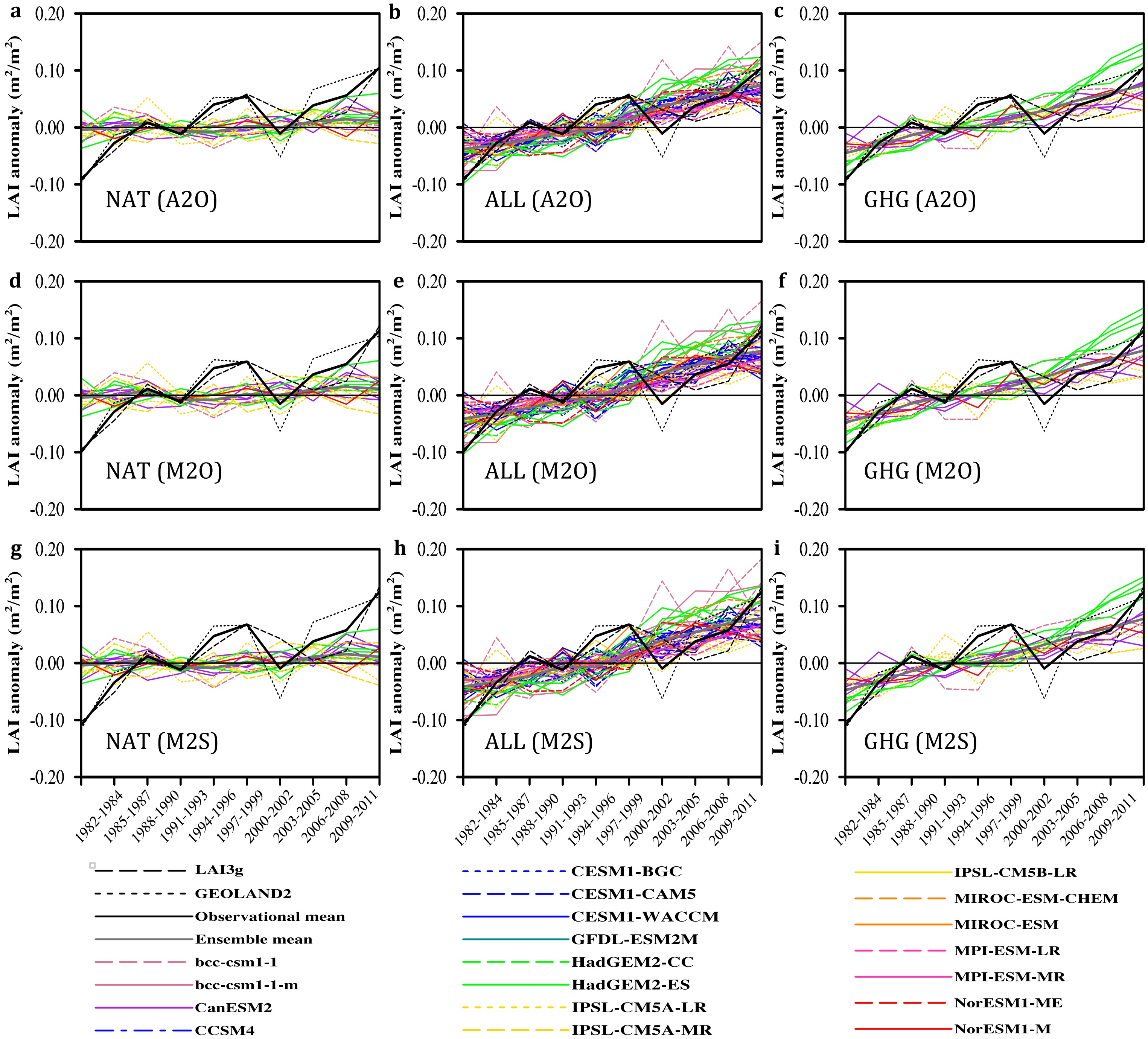

Figure S3.Observed and simulated 1982-2011 time series of LAI anomalies. The 3-year mean Growing Season (a–c for April–October [A2O], d–f for May–October [M2O], and g–i for May–September [M2S]) LAI anomalies (m^2/m^2) over land of the northern-extratropical latitudes (NEL) for the LAI3g product, GEOLAND2 product, mean of LAI3g and GEOLAND2, individual CMIP5 simulations accounting for solely natural forcings (NAT), and both anthropogenic and natural forcings (ALL), as well as CMIP5 simulations accounting for greenhouse gas forcings (GHG). Specific information on the model name and ensemble size of each model can be referred to Table S1.

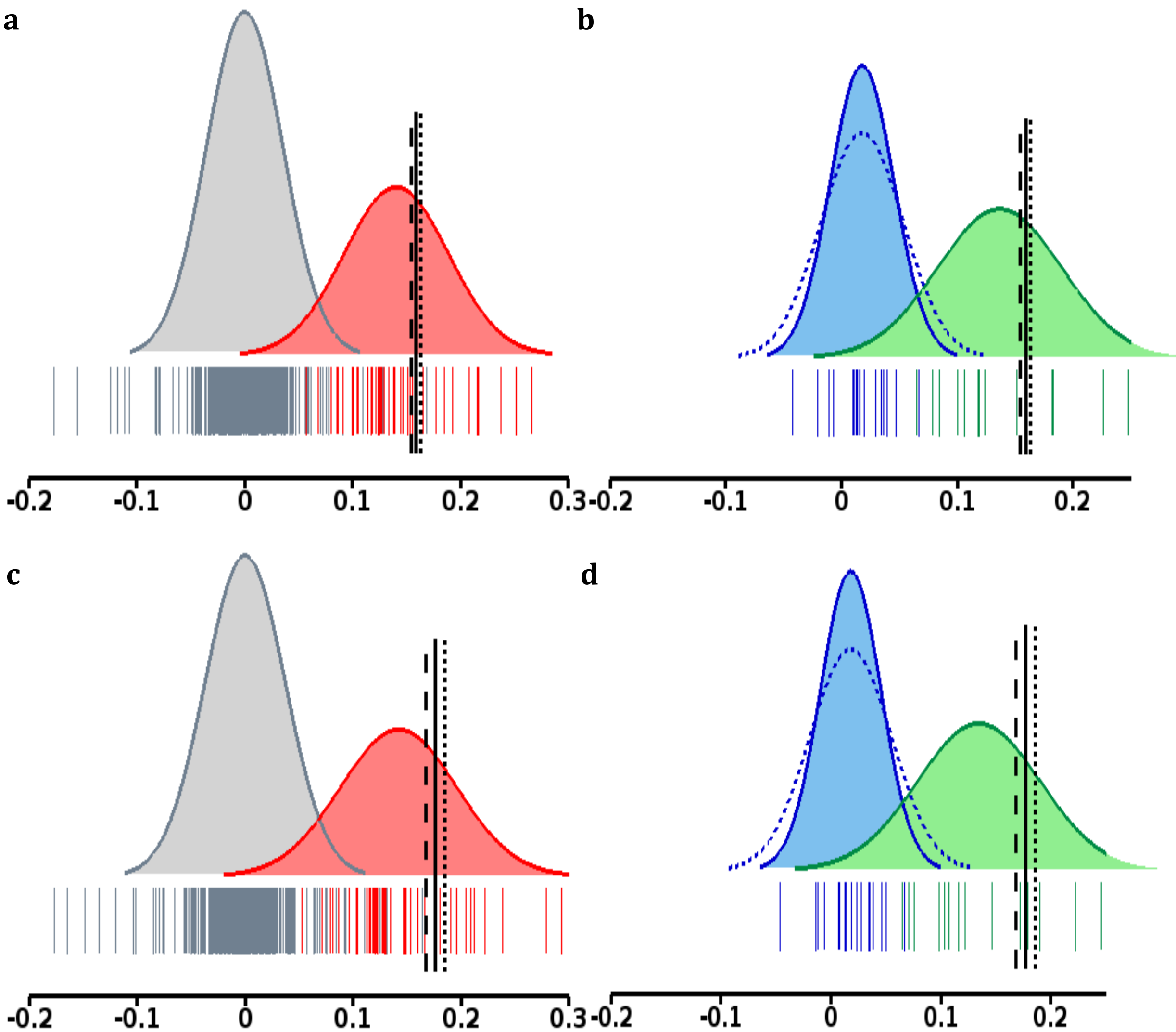

Figure S4. This is similar to Fig. 3, but considers different definitions of the growing season LAI (a and b for May–October [M2O], c and d for May–September [M2S]).

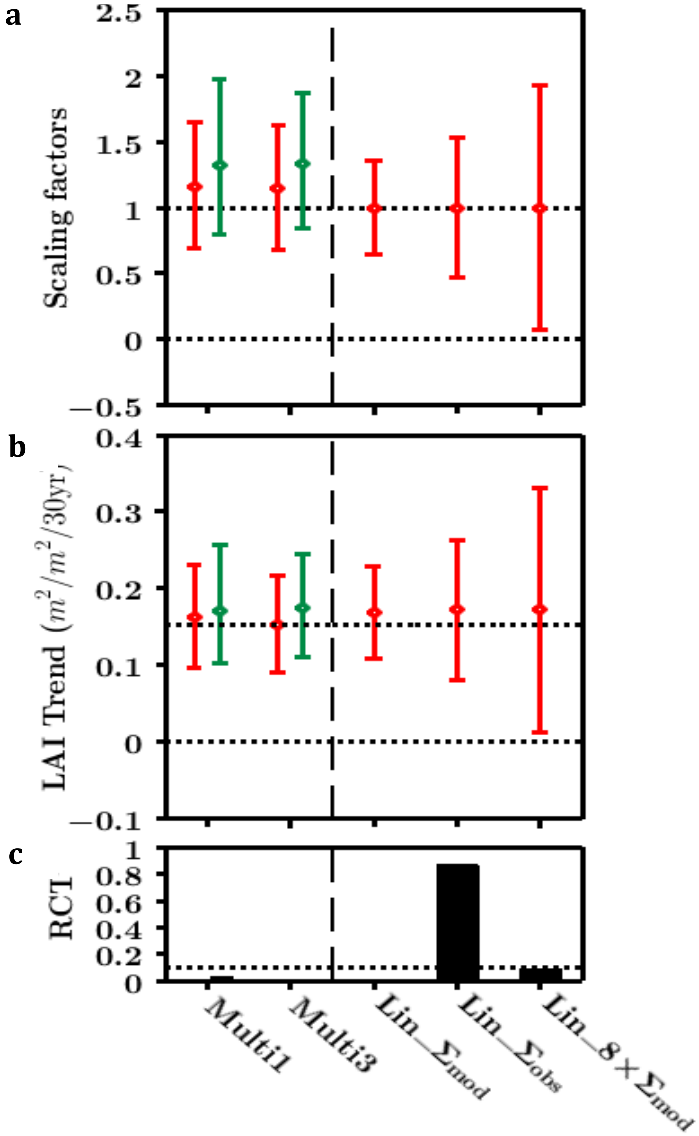

Figure S5: Sensitivity of optimal D&A to inflated variance assumptions. The optimal D&A analysis shown in Fig. 4 of the main text (Multi1 and Multi3 response patterns) is compared to results obtained considering a simplified method (linear trend and OLS fit, see text) and assuming an inflated IV. IV is estimated from unforced preindustrial simulations (Lin_Σmod), the observations (Lin_Σobs), or inflated arbitrarily by a factor of 8 (Lin_8xΣmod). Scaling factors, attributable trends, and the p-value of the residual consistency test are shown as being consistent with those in the Fig. 4.

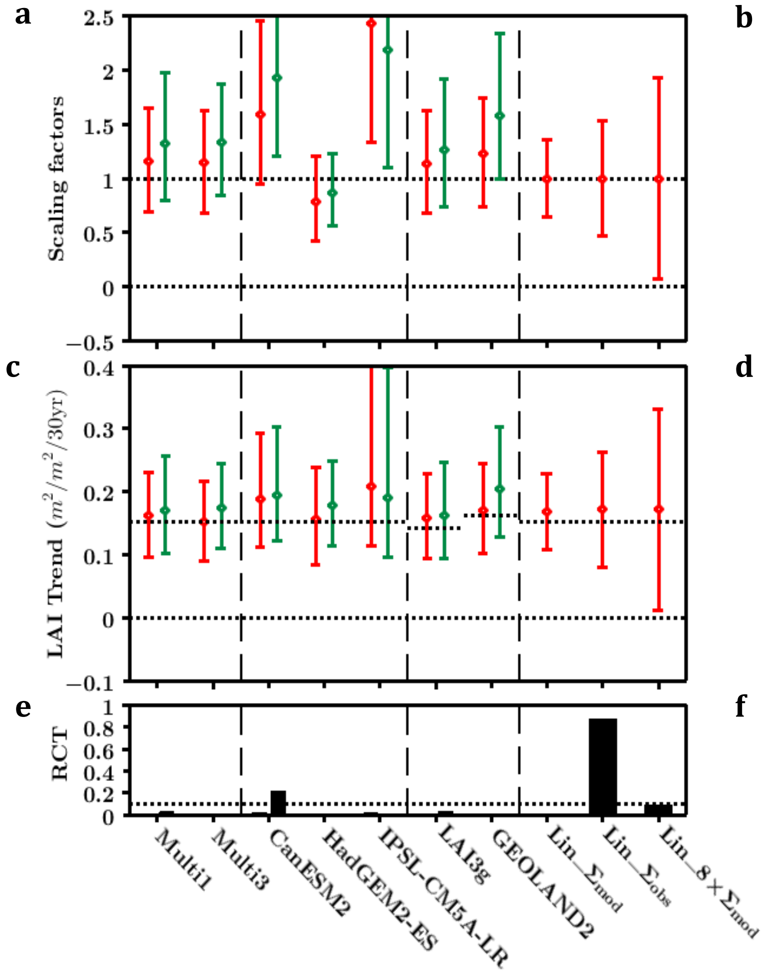

Figure S6. Results for the optimal D&A using alternative growing season definitions. This is similar to the merged Figs. 4 and S5, but considers different definitions of the growing season LAI (a, c, and e for May–October [M2O], b, d, and f for May–September [M2S]).

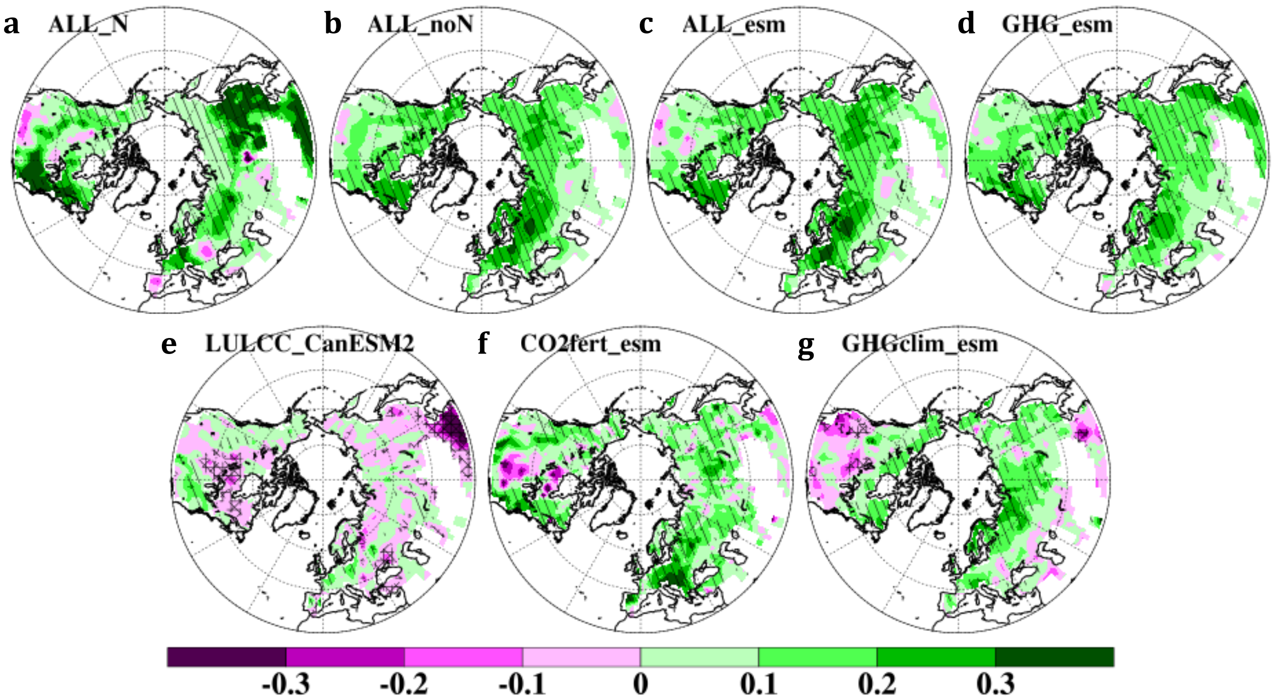

Figure S7. Spatial distribution of LAI trends for 1982–2011. Spatial distribution of the linear trends in the growing season (April–October) LAI ($m^2/m^2/30yr$) in

(a) CMIP5 simulations with anthropogenic and natural forcings for those models having dynamic nitrogen process (i.e., having the CLM4 model [ALL_N]),

(b) CMIP5 simulations with anthropogenic and natural forcings for those models having no dynamic nitrogen process (ALL_noN),

(c) CMIP5 simulations with anthropogenic and natural forcings for those models having esmFixClim2 (CO_2-induced physiological effects, radiation code sees constant CO_2 concentration of year 1850, but carbon cycle sees historical followed by RCP4.5 rise in CO_2) or esmFdbk2 (GHG-induced climate effects, carbon cycle sees constant CO_2 concentration of year 1850, but radiation sees historical followed by RCP4.5 rise in CO_2) experiments (ALL_esm),

(d) CMIP5 simulations with greenhouse gases forcings for those models having esmFixClim2 or esmFdbk2 experiments (GHG_esm),

(e) CanESM2 simulations with land use/land cover change only (LULCC_CanESM2),

(f) the esmFixClim2 simulations (CO2fert_esm), and

(g) the esmFdbk2 simulations (GHGclim_esm).

The hatched area indicates at least 90% of the simulation members agree on the increasing trend of LAI, and area with black crosses indicates at least 90% percent of the simulation members agree on the decreasing trend of LAI. These figures are designed to provide insights on the possible processes behind the anthropogenic impacts (e.g., nitrogen deposition, land use/land cover change, and the CO_2-induced physiological vs. GHG-induced climate effects) on the vegetation growth.

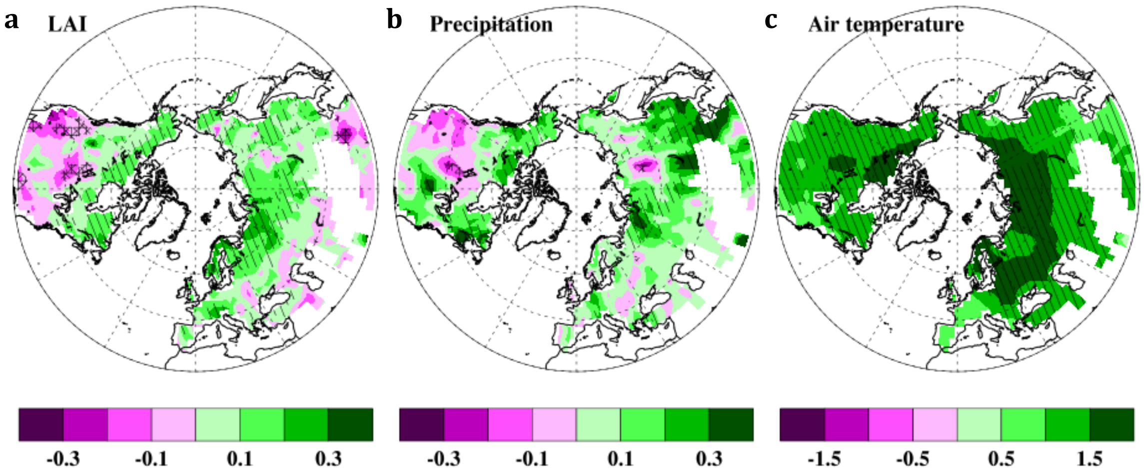

Figure S8. Spatial distribution of LAI, precipitation and temperature trends for 1982–2011. Spatial distribution of the trends in the growing season (April–October)
(a) climate-induced LAI ($m^2/m^2/30yr$),
(b) precipitation (mm/day/30yr), and
(c) temperature (°C/30yr) from the CMIP5 esmFdbk2 simulations (GHG-induced climate effects, carbon cycle sees constant CO_2 concentration of year 1850, but radiation sees historical followed by RCP4.5 rise in CO_2).
The hatched area indicates at least 90% of the simulation members agree on the increasing trends, and area with black crosses indicates at least 90% percent of the simulation members agree on the decreasing trends. The (a) is identical to that of Fig. S7g. These figures are designed to provide insights on the possible climatic drivers of LAI changes for the GHG-induced climate change shown in Fig. S7g.

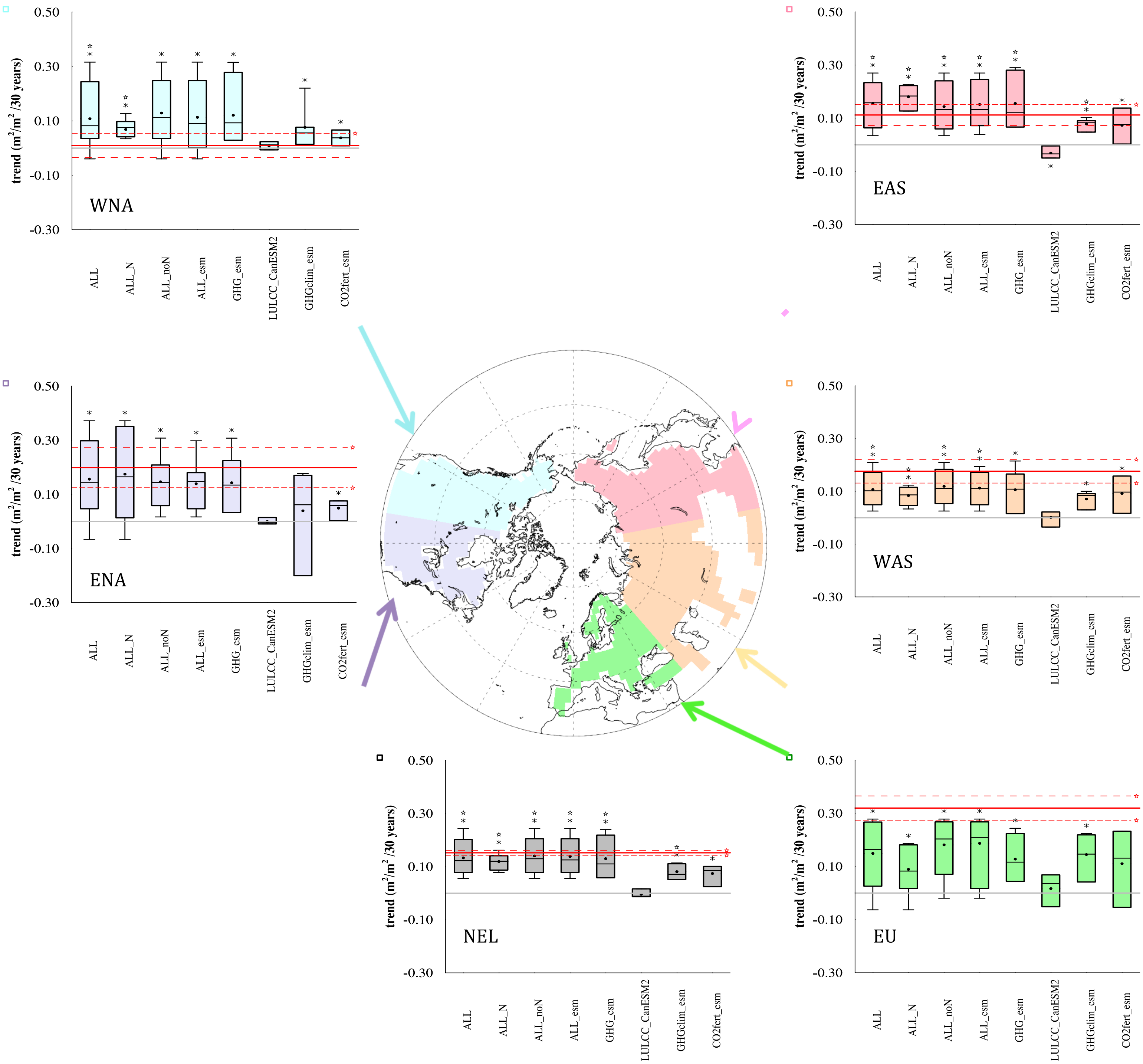
WNA
EAS
ENA
WAS
NEL
EU
trend (m2/m2 /30 years)
0.50
0.30
0.10
-0.10
-0.30
ALL
ALL_N
ALL_noN
ALL_esm
GHG_esm
LULCC_CanESM2
GHGclim_esm
CO2fert_esm

Figure S9. Regional summaries of LAI trends for 1982-2011. Linear trends in the growing season (April–October) LAI (m^2/m^2/30yr) of CMIP5 simulations with anthropogenic and natural forcings (ALL) CMIP5 simulations with anthropogenic and natural forcings for those models having dynamic nitrogen process, which means having the CLM4 model (ALL_N), CMIP5 simulations with anthropogenic and natural forcings for those models having no dynamic nitrogen process (ALL_noN), CMIP5 simulations with anthropogenic and natural forcings for those models having esmFixClim2 (CO_2-induced physiological effects, radiation code sees constant CO_2 concentration of year 1850, but carbon cycle sees historical followed by RCP4.5 rise in CO_2) or esmFdbk2 (GHG-induced climate effects, carbon cycle sees constant CO_2 concentration of year 1850, but radiation sees historical followed by RCP4.5 rise in CO_2) experiments (ALL_esm), CMIP5 simulations with greenhouse gases forcings for those models having esmFixClim2 or esmFdbk2 experiments (GHG_esm), CanESM2 simulations with land use/land cover change only (LULCC_CanESM2), the esmFixClim2 simulations, and the esmFdbk2 simulations over land of northern-extratropical latitudes (NEL), western North America (WNA), eastern North America (ENA), Europe (EU) and western Asia (WAS), and eastern Asia (EAS). Boxes indicate 10% and 90% percentiles and bars represent the minimum and maximum value of all ensemble runs. Median and mean values are shown by the bar and dot inside each box. Stars above/below bars indicate at least 90% of ensemble runs agree on positive/negative trends. In addition, the asterisks above/below bars indicate at least 90% of ensemble runs agree on significantly positive/negative trends. The two red dashed lines indicate the trends from LAI3g (short dash) and GEOLAND2 (long dash), and the solid red line shows the average trend of the two observations. A star is shown to the right end of each red dashed line if the trend is significantly positive. The grey solid line is the reference line across zero.